Origin of insulating and nonferromagnetic SrRuO₃ monolayers

Zeeshan Ali [1], Zhen Wang [1,3], Andrew O'Hara [2], Mohammad Saghayezhian [1], Donghan Shin,[2] Yimei Zhu [3,*]
Sokrates T. Pantelides [2,4,†] and Jiandi Zhang [1,5,‡]

[1]*Department of Physics & Astronomy, Louisiana State University, Baton Rouge, Louisiana 70803, USA*
[2]*Department of Physics and Astronomy, Vanderbilt University, Nashville, Tennessee 37235, USA*
[3]*Condensed Matter Physics & Materials Science, Department, Brookhaven National Laboratory, Upton, New York 11973, USA*
[4]*Department of Electrical Computer Engineering, Vanderbilt University, Nashville, Tennessee 37235, USA*
[5]*Beijing National Laboratory for Condensed Matter Physics, Institute of Physics, Chinese Academy of Sciences, 100190 Beijing, China*

The electromagnetic properties of ultrathin epitaxial ruthenate films have long been the subject of debate. Here we combine experimental with theoretical investigations of $(SrTiO_3)^5$-$(SrRuO_3)^n$-$(SrTiO_3)^5$ (STO^5-SRO^n-STO^5) heterostructures with $n = 1$ and 2 unit cells, including extensive atomic-resolution scanning-transmission electron-microscopy imaging, electron-energy-loss spectroscopy chemical mapping, as well as transport and magnetotransport measurements. The experimental data demonstrate that the STO^5-SRO^2-STO^5 heterostructure is nearly stoichiometric, metallic, and ferromagnetic with $T_C \sim 128$ K, even though it lacks the characteristic bulk-SRO octahedral tilts and matches the cubic STO structure. In contrast, the STO^5-SRO^1-STO^5 heterostructure features Ru-Ti intermixing in the RuO_2 layer, also without octahedral tilts, but is accompanied by a loss of metallicity and ferromagnetism. Density-functional theory calculations show that stoichiometric $n = 1$ and $n = 2$ heterostructures are metallic and ferromagnetic with no octahedral tilts, while nonstoichiometry in the Ru sublattice in the $n = 1$ case opens an energy gap and induces antiferromagnetic ordering. Thus, the results indicate that the observed nonstoichiometry is the cause of the observed loss of metallicity and ferromagnetism in the $n = 1$ case.

I. INTRODUCTION

Complex-oxide heterostructures have generated significant interest because of their diverse emergent phenomena, including ferromagnetism [1–3], ferroelectricity [4,5], interfacial 2D electron gas [6], topological spin texture [7], strain-induced superconductivity [8], etc. However, one limitation in the design of thin-film based oxide heterostructures is the occurrence of dead layers exhibiting insulating and nonferromagnetic behavior below a certain film thickness [9–11]. As a prototype example, bulk $4d$ transition-metal oxide $SrRuO_3$ (SRO) has an orthorhombic perovskite lattice structure [12] and a ferromagnetic (FM)-metal-metallic ground state with a Curie temperature of ∼160 K [13,14]. However, ultrathin films of SRO grown on substrates such as $SrTiO_3$ (STO) exhibit intriguing properties that are different from bulk counterparts [15–19], including the occurrence of metal-insulator transition (MIT) and non-FM state [11,20–24].

Historically, the earliest experimental investigation by Toyota *et al.* [25,26] initiated interest in thickness-dependent properties of SRO, where MIT is observed to arise at a film thickness of 4–5 unit-cells (u.c.). Nonetheless, different values

have since been reported for the MIT critical thickness, from 2 u.c. [11], to 3 u.c. [20,21,24], and 4 u.c. [27], with the variance usually attributed to the degree of disorder existing in films. Numerous theoretical studies have explored the origin of MIT, while remaining inconclusive regarding the critical thickness and nature of the ground state, i.e., whether FM or antiferromagnetic (AFM) insulator [28–31]. Several authors suggested that reducing film thickness may enhance electronic correlations [18,32,33] and result in a structural transition [34]. Rondinelli *et al.* [28], however, reported a comprehensive theoretical investigation of these effects and found that neither enhanced electronic correlations nor structural transitions could reproduce the experimentally observed MIT, leading to a suggestion that extrinsic effects (such as surface disorder and defects) or dynamic spin correlations may be the dominant factor. To overcome the surface-induced disorder, single-unit SRO in the form of $(SRO)^1 - (STO)^5$ superlattice geometry has been examined experimentally. However, different ground states of single-u.c. SRO superlattices are obtained, from a non-FM insulator [22,23] to FM insulator [35] to borderline FM metal [36]. They are in contrast to the theoretically suggested half-metallic state for 1-u.c. SRO layer confined within STO lattice [32].

In this paper, we report a combined experimental and theoretical investigation on $(SrTiO_3)^5$-$(SrRuO_3)^n$-$(SrTiO_3)^5$ (STO^5-SRO^n-STO^5) heterostructures ($n = 1, 2$ u.c.). Electric and magnetotransport measurements demonstrate that STO^5-SRO^1-STO^5 is insulating and non-FM, whereas

*zhu@bnl.gov
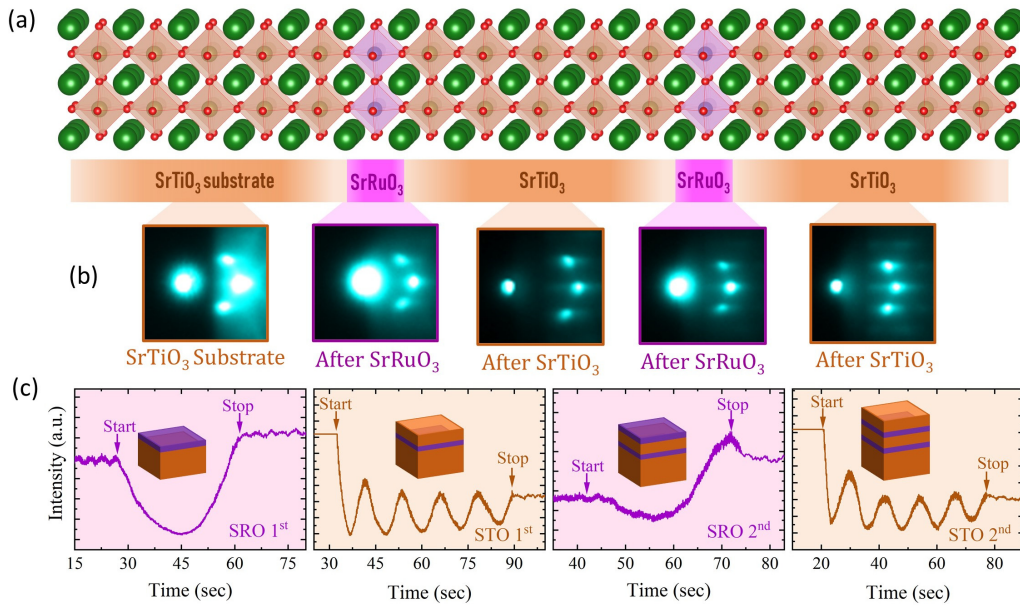†pantelides@vanderbilt.edu
‡jiandiz@iphy.ac.cn

FIG. 1. STO^5-SRO^1-STO^5 heterostructure: (a) schematic sketch, and (b) *in situ* RHEED patterns of STO substrate, SRO, and STO sublayers. (c) Time-dependent RHEED intensity profile.

STO^5-SRO^2-STO^5 is FM metallic with a Curie temperature of ~128 K. Atomically resolved structural analysis reveals that octahedral tilts are absent in both heterostructures, thus ruling out such structural changes as a controlling factor for such drastic property differences. On the other hand, atomically resolved electron-energy-loss spectroscopy (EELS) chemical maps show that STO^5-SRO^1-STO^5 is nonstoichiometric with substantial interface-induced Ti-Ru intermixture, while STO^5-SRO^2-STO^5 is nearly stoichiometric. Density-functional theory (DFT) calculations find that stoichiometric STO^5-SRO^n-STO^5 ($n = 1, 2$ u.c.) are still FM metallic without SRO octahedral tilts. Ru deficiency caused by Ti-Ru intermixing leads to the stabilization of AFM ordering and insulating behavior in the monolayer SRO indicating that the experimentally observed intermixing is indeed responsible for the observed loss of metallicity and ferromagnetism.

II. EXPERIMENT

A. Thin-film growth

Heterostructures of the form STO^5-SRO^n-STO^5 with $n = 1, 2$ u.c. [see Fig. 1(a)] were fabricated via pulsed-laser deposition on $SrTiO_3$ (STO) substrates oriented with a (001) surface. Both STO^5-SRO^1-STO^5 and STO^5-SRO^2-STO^5 heterostructures have two repetitions of SRO/STO building blocks. The STO substrates were first sonicated in deionized water and then treated for 30 s in buffered hydrogen fluoride, followed by annealing at 950 °C in an oxygen atmosphere to produce atomically smooth surfaces. The SRO and STO films were grown at 650 °C with an oxygen pressure of 100 and 10 mTorr, respectively. A KrF excimer laser ($\lambda = 248$ nm) laser repetition with a rate of 10 Hz (SRO) and 5 Hz (STO), and energy of 300 mJ (SRO) and 260 mJ (STO) was used. Post deposition, the samples were cooled down at ~12 °/min to room temperature in 100-mTorr oxygen. The film thickness was

monitored by *in situ* reflection high-energy electron diffraction (RHEED). Figures 1(b) and 1(c) show *in situ* RHEED results. Time-dependent RHEED oscillations show stabilized layer-by-layer film-growth mode throughout the deposition process [see Fig. 1(c)]. Moreover, the RHEED pattern of SRO and STO sublayers indicate an atomically smooth film surface [Fig. 1(b)].

B. Electrical transport and magnetic property measurements

Electron transport measurements were performed via a Quantum Design physical property measurement system in a four-probe configuration. The magnetoresistance (MR) was measured at different temperatures by applying an external magnetic field along film normal. The samples magnetization was studied by using a Quantum Design superconducting quantum interference device (SQUID) reciprocating sample option. The magnetization as a function of temperature $M(T)$ measurement was obtained via first cooling the samples down to 5 K under the 0.2 T field, and then while warming in presence of 0.01 T, the $M(T)$ data was collected.

C. Scanning transmission electron microscopy and EELS

Scanning transmission electron microscopy (STEM) and EELS experiments were performed on a 200-kV JEOL ARM electron microscope at Brookhaven National Library equipped with double-aberration correctors, a dual energy-loss spectrometer, and a cold field-emission source. TEM samples were prepared using a focused ion beam with Ga^+ ions followed by Ar^+ ions milling to a thickness of ~30 nm. The atomic-resolution STEM images were collected with a 21-mrad convergent angle (30-μm condenser aperture) and a collection angle of 67–275 mrad for high-angle annular dark-field (HAADF) and 11–23 mrad for annular bright-field (ABF) imaging. The atomic positions were obtained using
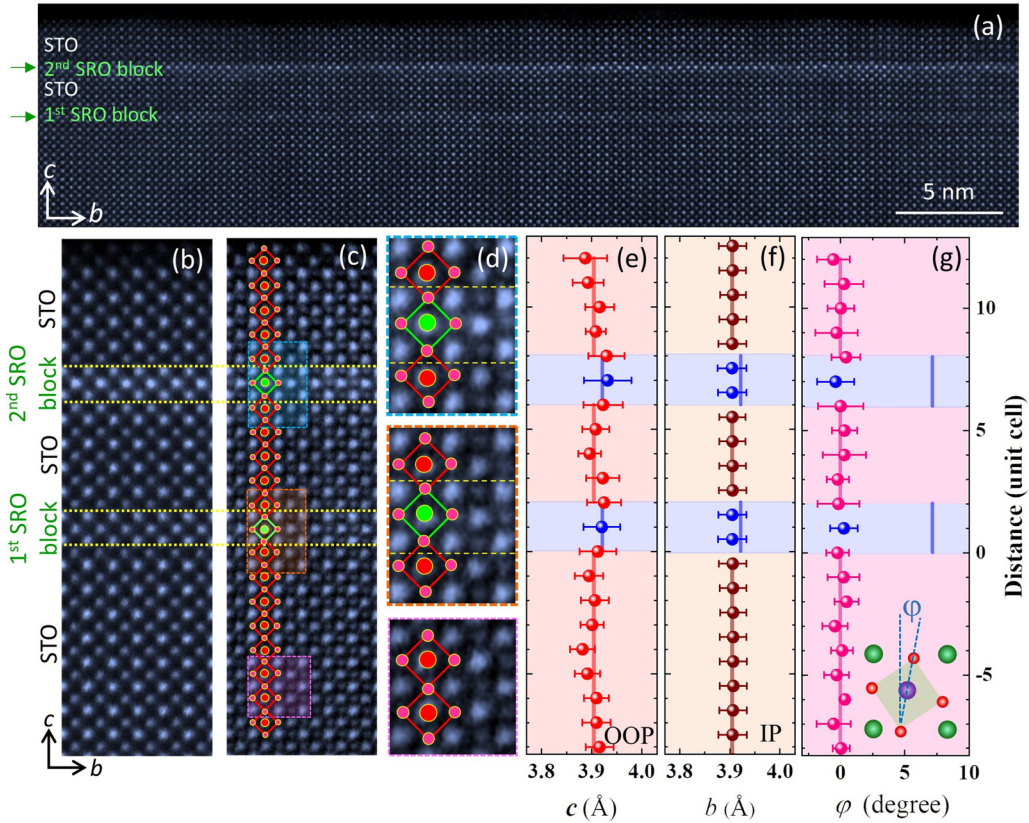
FIG. 2. Atomically resolved structure of STO^5-SRO^1-STO^5 (with two repeating blocks of single-u.c. SRO) viewed along the [100] direction: (a) large-area HAADF-, (b) high-magnification HAADF-, (c) intensity-inversed ABF, and (d) zoomed inversed ABF-STEM images. The dotted orange line marks the interface, whereas red and green squares in panel (c-d) signify the projected octahedral shapes in STO and SRO. (e) Out-of-plane and (f) in -plane lattice parameter c and b, respectively, as a function of distance from the film-substrate interface. The error bar shows the standard deviations of the averaged measurements along the b axis. The pseudocubic lattice parameters of bulk STO ($a_{STO} = 3.905$ Å) and SRO ($a_{SRO} = 3.925$ Å) are indicated by a red and blue solid line, respectively. (g) Variation of projected octahedral tilt angle (φ). The definition of φ is specified in the inset. The solid blue line in panel (g) marks the φ in bulk SRO ($\sim 7.2°$). No octahedra tilts across the interfaces are observed.

two-dimensional Gaussian fitting following the maximum intensity. The microscope conditions were optimized for EELS acquisition with a probe size of 0.8 Å, a convergence semiangle of 20 mrad, and a collection semiangle of 88 mrad. Dual EELS mode was used to collect low-loss and core-loss spectra simultaneously for energy drift calibration in the collecting process. EELS mapping was obtained across the whole film with a step size of 0.2 Å and a dwell time of 0.05 s/pixel. The EELS background was subtracted using a power-law function, and multiple scattering was removed by a Fourier deconvolution method.

III. RESULTS AND DISCUSSION

A. Structure and composition

The structure and composition of the samples were investigated via atomic-resolution HAADF/ABF-STEM imaging and EELS mapping. The intensity in the HAADF image is roughly proportional to $Z^{\sim 2}$ (Z is an atomic number), depicting directly heavy-atom positions, whereas ABF imaging is useful for visualization of lighter atoms such as oxygen. The STEM images of STO^5-SRO^1-STO^5 with two repeating blocks of single-u.c. SRO are shown in Fig. 2. The individual

Sr ($Z = 38$), Ru ($Z = 44$), and Ti ($Z = 22$) atoms could be distinguished based on intensity contrast [see Figs. 2(a)–2(d)], permitting us to determine the heterointerfaces [see yellow lines in Figs. 2(b)–2(d)]. The HAADF-STEM images reveal that the crystalline lattice is coherent across the interfaces in the entire heterostructure. Furthermore, it can be seen from the HAADF image that the Ru column in the first SRO block is darker than that in the second SRO block, which is related to severe Ti-Ru intermixing as will be discussed later.

To quantitatively examine the lattice-mismatch induced structural distortions, we determined the out-of-plane (OOP) and in-plane (IP) lattice parameters from A-site atomic positions [see Figs. 2(e) and 2(f)]. The IP lattice parameter (b) of the SRO/STO interlayer is consistent with the STO substrate [Fig. 2(f)], indicating the sublayers are fully compressively strained (bulk: $a_{STO} = 3.905$ Å and $a_{SRO} = 3.925$ Å). The OOP lattice parameter (c) of the SRO blocks [Fig. 2(e)] is nearly the same as that of STO, suggesting a cubic symmetry, but the octahedral volume is smaller (59.85 ± 0.09 Å^3) than the bulk SRO (~ 60.37 Å^3) value of RuO_6, which is associated with Ti-Ru intermixture (discussed later).

Furthermore, in the ABF image [Figs. 2(c) and 2(d)] of the STO^5-SRO^1-STO^5 heterostructure, oxygen columns are

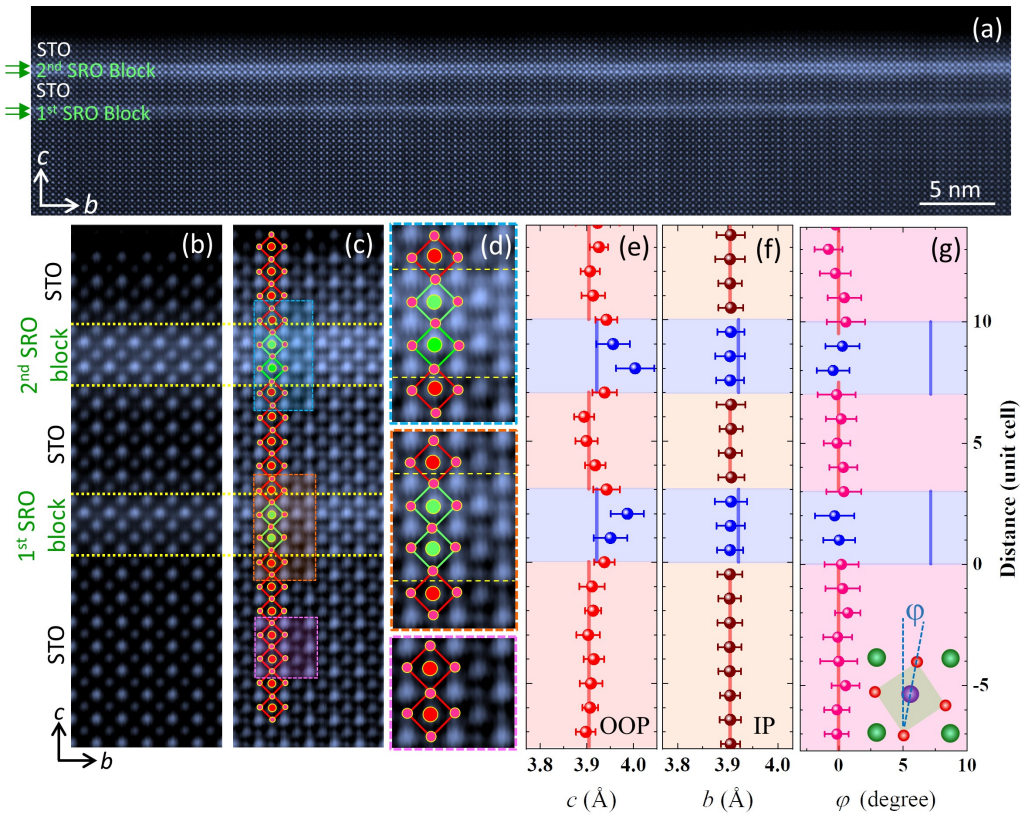FIG. 3. Atomically resolved structure of STO^5-SRO^2-STO^5 (with two repeating blocks of 2 u.c. SRO) viewed along the [100] direction: (a) large-area HAADF-, (b) high-magnification HAADF-, (c) intensity-inversed ABF, and (d) zoomed inversed ABF-STEM images. The dotted orange line marks the interface, whereas red and green squares in panel (c-d) signify the projected octahedral shapes in STO and SRO. (e) Out-of-plane and (f) in-plane lattice parameter c and b, respectively, as a function of distance from the film-substrate interface. The error bar shows the standard deviations of the averaged measurements along the b axis. The pseudocubic lattice parameters of bulk STO ($a_{STO} = 3.905$ Å) and SRO ($a_{SRO} = 3.925$ Å) are indicated by a red and blue solid line, respectively. (g) Variation of projected octahedral tilt angle (φ). The definition of φ is specified in the inset. The solid blue line in panel (g) marks the φ in bulk SRO ($\sim 7.2°$). No octahedra tilts across the interfaces are observed.

visible, hence permitting us to determine the octahedral geometry. We have determined the projected octahedral tilt angle (φ) as a function of atomic distance [see Fig. 2(g)]. The definition of φ is shown in the inset of Fig. 2(g). The φ [see Fig. 2(g)] of SRO and STO interlayers are nearly constant (averaged $\varphi \approx 0.37° \pm 1.2°$) and comparable to the value of STO substrate ($\varphi \approx 0.27° \pm 1.07°$), suggesting that the RuO$_6$ octahedral tilt is completely suppressed, while the projected RuO$_6$ octahedra are illustrated with the red/green box in Figs. 2(c) and 2(d).

The atomic-level view of the STO^5-SRO^2-STO^5 heterostructure with two repeating blocks of 2 u.c. SRO is shown in Fig. 3. The STEM images show coherent growth of the film where the two 2-u.c. SRO blocks are marked in Figs. 3(a)–3(d). Additionally, the trend of having a nearly constant IP lattice parameter (*b*) reiterates that the SRO/STO interlayers are epitaxially strained [Fig. 3(f)], ensuring a high-quality heterostructure. The OOP lattice parameter (*c*) of the STO layer follows its bulk value [Fig. 3(e)], while the SRO blocks show increased OOP lattice parameter due to compressive strain, suggesting a tetragonal symmetry. This OPP lattice parameter (*c*) in 2-u.c. SRO blocks are also larger than that of monolayer SRO heterostructure [see Fig. 2(e)], which will be

discussed later. On the other hand, for the STO^5-SRO^2-STO^5 heterostructure, the SRO block maintains an average octahedral tilt angle of $\varphi \approx 0.26° \pm 1.3°$ [as opposed to bulk SRO $\varphi \sim 7.2°$, see Fig. 3(g)], whereas the observed φ of SRO interlayer is similar to the φ prevailing in the STO substrate ($0.25° \pm 1.15°$). Given that octahedral units preserve their connectivity via corner-shared oxygen atoms, the ultrathin SRO confinement between cubic STO blocks facilitates the entire suppression of RuO$_6$ octahedral tilt angle, leading to stabilization of the artificially engineered bond angle of SRO [37–39].

To determine the possible *B*-site cation (Ti, Ru) intermixing in the heterostructures, we took and analyzed STEM/EELS maps from many areas of the samples. The results are presented in Fig. 4. As shown in Figs. 4(a)–4(c), the Ti atoms diffuse significantly into the Ru sites in STO^5-SRO^1-STO^5, especially the first SRO block (i.e., a single RuO$_2$ layer), resulting in the low Ru column intensity in the HAADF image [see Fig. 4(a)]. Quantitatively, the dopant Ti concentrations at the Ru sites were obtained from EELS profiles using the Lorentz-function fitting method, with the Ti in the STO substrate as reference. We note a $61 \pm 6\%$ Ti occupying the Ru site in the first (near-substrate) SRO block
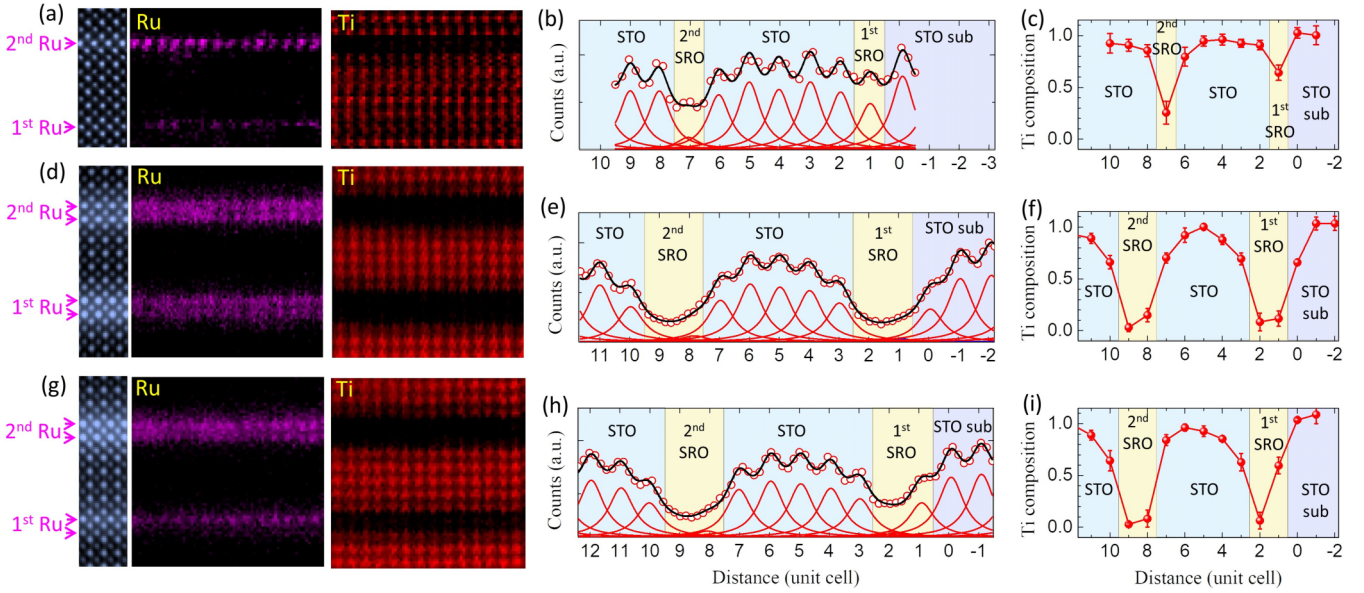
FIG. 4. STEM/EELS maps and elemental concentration: (a) HAADF images and EELS elemental maps from Ti-$L_{2,3}$, and Ru-$M_{2,3}$ edges, (b). (b) Least-squares fit of Ti EELS intensity profiles (red dots) from averaging the Ti maps over the horizontal direction in (a), and (c) Ti composition profiles across STO^5-SRO^1-STO^5 heterostructure. The black curve is a sum of the Lorentzian peaks fixed at the Ti lattice sites. The Lorentzian peaks indicate Ti concentration. The same arrangement of STEM/EELS characterization for two representative mapping areas of STO^5-SRO^2-STO^5 heterostructure, (d)–(f) and (g)–(i), respectively. The distance (in u.c.) is defined with respect to the film-substrate interface.

and $25 \pm 11\%$ in the second block of the STO^5-SRO^1-STO^5 heterostructure [see Figs. 4(b) and 4(c)]. On the other hand, the EELS mapping results from two representative areas of STO^5-SRO^2-STO^5 [one shown in Figs. 4(d)–4(f) and the other in Figs. 4(g)–4(i), respectively] are rather different from STO^5-SRO^1-STO^5. However, the Ti concentration is still significant and varies from one region to another in the RuO_2 layer proximal to STO substrate of the first SRO block [$\sim 10\%$ or less as in Fig. 4(f) to 60% as in Fig. 4(i)]. Nevertheless, few Ti ions ($\leqslant 10\%$) diffuse into the second RuO_2 layer of the first SRO block or both RuO_2 layers of second SRO blocks [see Figs. 4(d)–4(i)]. Overall, the spectroscopic observations suggest that the 2-u.c. SRO blocks in STO^5-SRO^2-STO^5 are nearly stoichiometric, while the single-u.c. SRO blocks in STO^5-SRO^1-STO^5 hold a higher Ru-cation off stoichiometry due to interface intermixture. The substantial Ti atoms in the single-u.c. SRO blocks of the STO^5-SRO^1-STO^5 heterostructure bring the OOP lattice parameter (c) of SRO close to that of STO [Fig. 2(e)]. Additionally, the RuO_6 octahedral volume is reduced ($59.85 \pm 0.09 \, \text{Å}^3$) in comparison to the bulk SRO ($\sim 60.37 \, \text{Å}^3$) (STO bulk volume: $59.45 \, \text{Å}^3$). In contrast, owing to nearly stoichiometric Ru concentration, the SRO blocks in STO^5-SRO^2-STO^5 retain their bulk-like pseudocubic unit-cell nature. Because of the in-plane compressive strain, the RuO_6 in STO^5-SRO^2-STO^5 shows slight elongation in the c axis [see Fig. 3(e)] while maintaining RuO_6 octahedral volume ($60.45 \pm 0.19 \, \text{Å}^3$) close to that in bulk SRO ($\sim 60.37 \, \text{Å}^3$). In ultrathin oxide ABO_3 heterostructures, the interface B-site intermixture is unavoidable, irrespective of the growth method [40]. In fact, sensitivity of ruthenates to B-site disorder and volatile nature of Ru makes it challenging to attain stoichiometric Ru films in the ultrathin limit [41–43].

B. Transport and magnetic properties

After a thorough understanding of the structure and composition, we proceed to investigate the transport and magnetotransport properties. Figure 5 shows sheet resistance as a function of the temperature of STO^5-SRO^n-STO^5 ($n = 1, 2$ u.c.) heterostructures. An insulating behavior of increasing resistance with lowering temperature is observed in
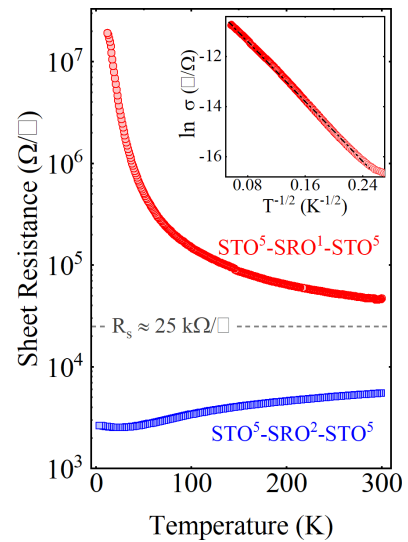

FIG. 5. Temperature-dependent sheet resistance of STO^5-SRO^n-STO^5 with $n = 1, 2$. The inset shows a logarithmic plot of STO^5-SRO^1-STO^5 conductivity vs $T^{-1/2}$, representing the Efros-Shklovskii variable-range hopping model. The gray dashed line is the quantum of resistance ($R_s \approx 25 \, k\Omega/\square$).
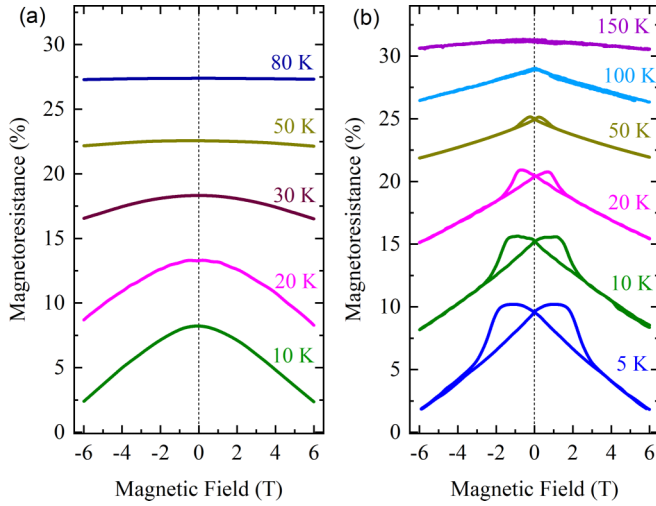
FIG. 6. Magnetoresistance of (a) STO^5-SRO^1-STO^5 and (b) STO^5-SRO^2-STO^5 measured at different temperatures.

STO^5-SRO^1-STO^5. Moreover, as shown in the inset of Fig. 5, the transport of STO^5-SRO^1-STO^5 can be fitted nicely with Efros-Shklovskii variable-range hopping model, where conductivity follows: $\sigma(T) = \sigma_0 e^{(T_{ES}/T)^{1/2}}$, $T_{ES} = \beta_{ES}\ e^2/\varepsilon\ k_B\ \xi$ is a characteristic temperature, ξ is localization length, e is elementary charge, ε is dielectric constant [44,45]. The linear fitting of data yields $T_{ES} \approx 900$ K, signifying the disorder-induced strong localization due to the Ti-Ru intermixture is likely the primary driving force for the insulating behavior. In the presence of strong localization effects, the kinetic theory of conductivity ($\sigma = e^2 k_F l/h$, where k_F is Fermi wave vector, and l is mean-free path) breaks down, since the electronic mean-free path (l) turns out to be equal to lattice spacing ($l \approx a$), leading to $k_F l \approx 1$, and the system crosses the minimum metallic conductivity known as the Ioffe-Regel limit [46,47], where the sheet resistance limit is $R_s = h/e^2$ 25 kΩ/$\square$. Figure 5 confirms that the STO^5-SRO^1-STO^5 heterostructure sheet resistance exceeds the Ioffe-Regel limit in the measured temperature range. On other hand, the STO^5-SRO^2-STO^5 heterostructure shows a metallic character (see Fig. 5) in the measured temperature range. However, the small resistivity upturn below $\sim$25 K is observed, mainly caused by the disorder-induced weak localization effects [9,27,48].

We have performed magnetoresistance (MR) measurements: MR = {$\rho(H)$-$\rho(0)$}/$\rho(0)$; here $\rho(H)$ and $\rho(0)$ are resistivities in the presence and absence of a magnetic field, respectively [the external magnetic field (H) is perpendicular to the film plane]. The MR of STO^5-SRO^1-STO^5 shows a parabolic nature [Fig. 6(a)], signifying an absence of FM order. In contrast, the MR of STO^5-SRO^2-STO^5 shows a butterfly loop MR, representing the FM state [Fig. 6(b)]. The maximum ($\sim$2 T) in the MR at 5 K hysteretic curve corresponds to coercive field H_c, whereas the point of forward and backward sweeps overlapping is the saturation field ($\sim$6 T). The hysteretic MR characteristic of FM ordering persists up to $\sim$55 K, though nonparabolic MR dependence continues up to $\sim$120 K. For manganites [49–52], granular magnetic systems [53,54], and SRO [55], the MR scales as MR $\propto [M(H)/M_s]^2$, while MR $\propto [\mu_0 H]^2$ for nonmagnetic-conducting systems
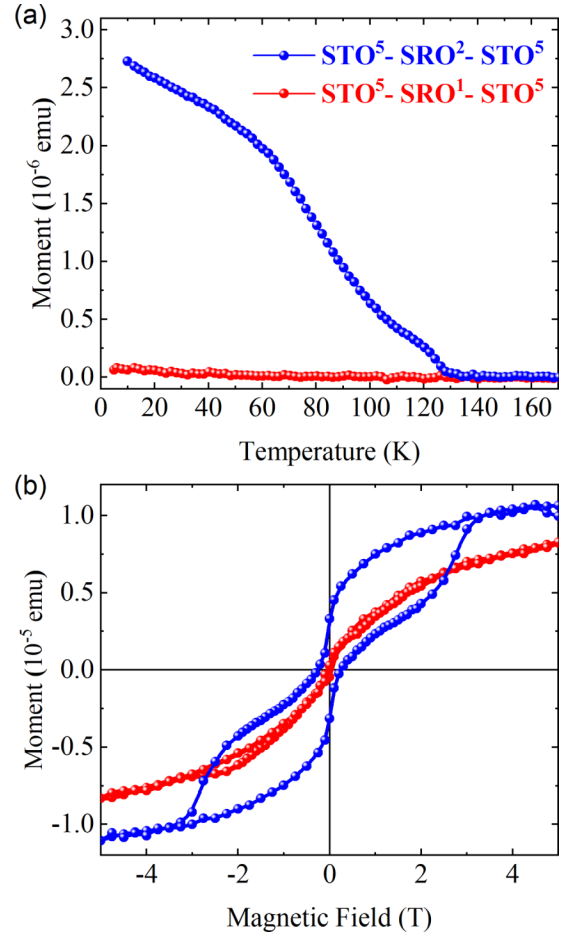

FIG. 7. STO^5-SRO^n-STO^5 [$n = 1, 2$]: (a) Temperature-dependent magnetization and (b) magnetic hysteresis measured at 5 K.

[36,53,56], where M_S is saturation magnetization and H the applied field. The magnetoresistance dependence on the magnetization (MR $\propto M^2$) suggests that electron transport depends on the magnetic moment's alignment within magnetic domains. As the magnetic moments are aligned, the carrier scattering decreases and so does the resistivity, while the resistivity is maximized at the coercive fields. Yet, trapping centers such as dislocations, defects, and nonmagnetic inhomogeneity might cause the pinning of domain walls, leading to enlarged switching fields [56]. Moreover, the disappearance of the butterfly loop before the actual T_C is triggered by the dominance of thermal fluctuations over the pinning of domain walls [36,53,56]. Nonetheless, the presence of a butterflylike feature in the MR below 55 K corroborates the presence of FM ordering in STO^5-SRO^2-STO^5, while the single-u.c. SRO is non-FM.

The magnetization of STO^5-SRO^n-STO^5 ($n = 1, 2$ u.c.) heterostructures was also studied via SQUID magnetometry. To measure magnetization as a function of temperature $M(T)$, the samples were first cooled down to 5 K under the 0.2 T field, and then while warming in the presence of 0.01 T, the data was collected. The STO^5-SRO^1-STO^5 does not show any sign of FM transition, as the $M(T)$ curve is nearly flat [see Fig. 7(a)], and the $M(H)$ is reminiscent of background
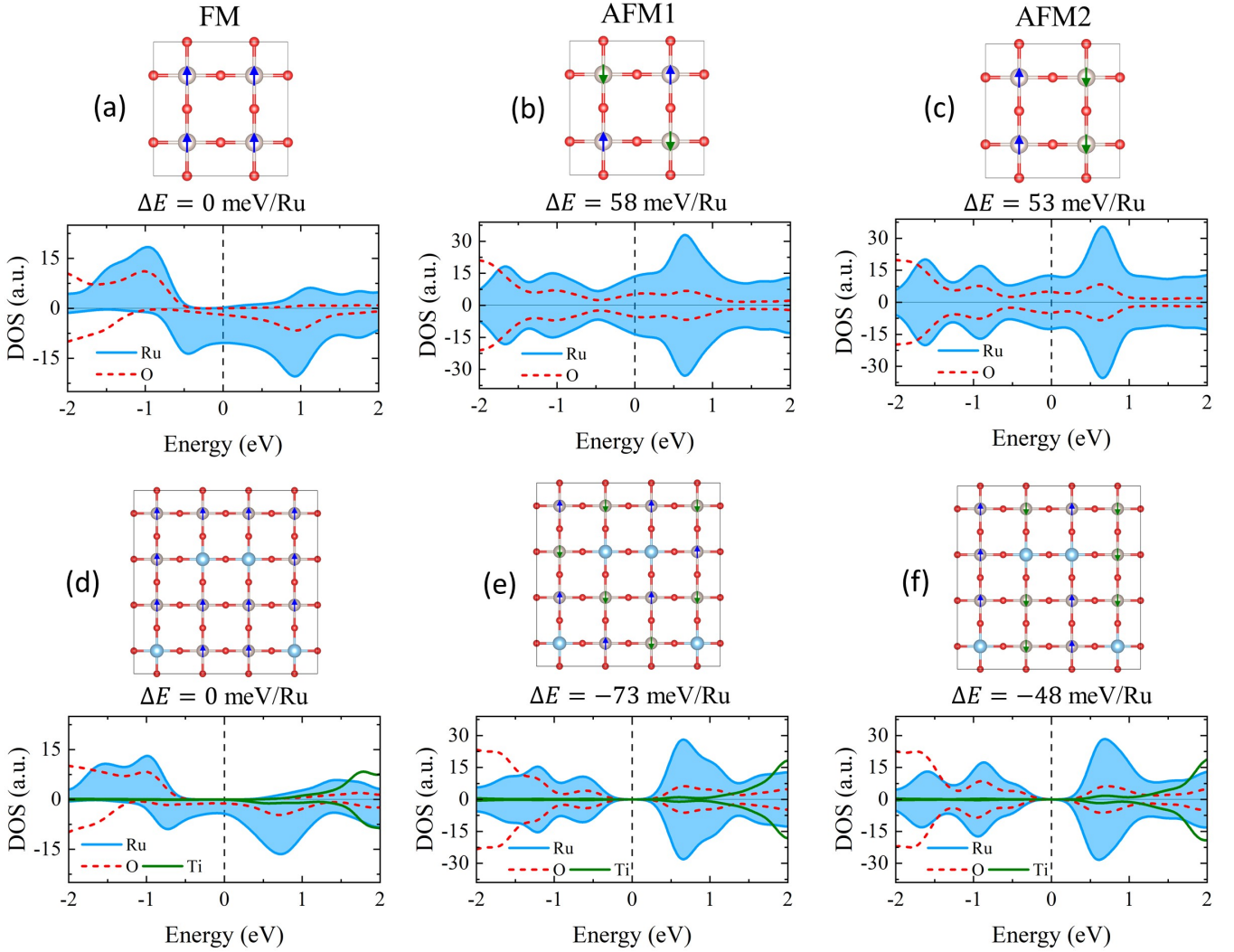
FIG. 8. Magnetic arrangements (top) and projected density of states (bottom) for the RuO_2 planes in STO^5-SRO^1-STO^5 heterostructures. Panels (a)–(c) are for a heterostructure containing a stoichiometric RuO_2 plane. Panels (d)–(f) are for 25% substitution of Ti for Ru within the RuO_2 plane. All densities of states are normalized to the same lateral system size so that they can be compared.

hysteresis of the substrate [Fig. 7(b)], verifying the absence of FM state. However, STO^5-SRO^2-STO^5 exhibits robust FM ordering as shown by sharp paramagnetic to FM transition at $T_C \sim 128$ K in $M(T)$ [Fig. 7(a)] and characteristic ferromagnetic hysteresis [see $M(H)$ in Fig. 7(b)]. Overall, the electron transport and magnetic properties results indicate that the presence of metallicity is important for stabilizing ferromagnetism since an insulating SRO is nonmagnetic.

C. DFT calculations of intrinsic and extrinsic heterostructures

In order to better understand the magnetic and electronic nature of the present heterostructures, we have performed DFT calculations on STO^5-SRO^n-STO^5 ($n = 1, 2$ u.c.) heterostructures (see the Appendix for computational details). The structural calculations reveal that both STO^5-SRO^1-STO^5 and the STO^5-SRO^2-STO^5 heterostructures feature nontilted octahedra in the SRO layers, in accord with the STEM data (see Figs. 2 and 3). Thus, both experiments and theory rule out structural distortions to

be the regulatory factor for the observed contrasting electromagnetic (see Figs. 5–7) properties in the two heterostructures.

Beginning with the STO^5-SRO^1-STO^5 system, there are three possible magnetic arrangements for the Ru spins as shown in Fig. 8(a) FM; Fig. 8(b) checkerboard AFM (AFM1); and Fig. 8(c) striped AFM (AFM2). The FM order is the ground state by 53 meV per Ru atom. In this FM state, the SRO layer in the STO^5-SRO^1-STO^5 system is half metallic, namely metallic in only the minority-spin polarized electrons, while a gap appears between the spin-up t_{2g} and e_g states [see Fig. 8(a)]. In contrast, both the higher-energy AFM phases are metallic as shown by the density of states in Figs. 8(b) and 8(c). The FM metallic ground-state results are consistent with prior literature [32,33] and indicate that the observed non-FM insulating state is likely due to extrinsic effects and is not an intrinsic property of the system [28].

As demonstrated by the STEM results in Figs. 4(a)–4(c) of STO^5-SRO^1-STO^5 heterostructure, the first SRO and second SRO blocks contain $61 \pm 6\%$ to $25 \pm 11\%$ Ru deficiency by

Ti-for-Ru substitution, respectively. Therefore, from the original STO^5-SRO^1-STO^5 heterostructure model, we constructed a lateral heterostructure containing 16 Ru sites and replace four of them with Ti to achieve 25% Ru deficiency via substitution. The chosen arrangement shown in Figs. 8(d)–8(f) allows consideration of the same basic FM and AFM arrangements as before. We find that the introduction of the Ti leads to the energetic stabilization of both AFM arrangements relative to the FM solution. Furthermore, as seen in the density of states plots of Figs. 8(d)–8(f), the introduction of Ti within the RuO_2 layer leads to shifts in the oxygen/transition-metal hybridization and opens a band gap of 0.4 eV for both AFM orderings. Thus, we can conclude that the introduction of Ti within the RuO_2 layer via interfacial intermixture observed in STEM (see Fig. 4) is responsible for the observed magnetic and electronic properties shown in Figs. 5, 6(a), and 7. This result complements the report by Boschker *et al.* [36], where using adsorption-controlled molecular-beam epitaxy, the SRO in monolayer limit is unveiled to hold metallicity and FM order, echoing the importance of the role of interface-induced intermixing and impurities in determining heterostructure properties [40,42,43,57]. Although other Ti-for-Ru substitutional patterns are possible, these calculations become prohibitively expensive with current methods. For this reason, we did not explore if a critical percent substitution of Ti-for-Ru exists that can maintain FM and metallicity. Nevertheless, if defects are eradicated, a metallic-FM monolayer SRO could be stabilized [36].

For the STO^5-SRO^2-STO^5 heterostructure, we consider four possible AFM arrangements [see the top of Fig. 9(a)] based on the prior single-layer AFM arrangements (with differing coupling along the c axis of the heterostructure) as well as an additional arrangement (AFM7) which has FM ordering within each plane. For AFM3 through AFM6, the total relative energy per Ru atom is much higher than the FM order compared to the stoichiometric STO^5-SRO^1-STO^5 case [see Fig. 9(a)]. The AFM7 case is also found to be higher in energy than the FM ordering, but is lower than the other STO^5-SRO^2-STO^5 energies since only the interlayer exchange coupling energy plays a role in the ΔE. As expected, the density of states for the RuO_2 layers [the lower layer is shown in Fig. 9(b); the upper layer looks similar] remains metallic like stoichiometric STO^5-SRO^1-STO^5 structure and consistent with the experimental results shown in Figs. 5, 6(b), and 7.

IV. CONCLUSIONS

In conclusion, by fabricating artificial heterostructures of the form STO^5-SRO^n-STO^5 ($n = 1, 2$ u.c.), we have shown that the heterostructure with 2-u.c. SRO is metallic and FM ($T_C \sim 128$ K) while the heterostructure with single-u.c. SRO is insulating and non-FM. There is no fundamental change in lattice structure with reducing the thickness of SRO, thus excluding structural modification as a controlling factor for such drastic property transitions. DFT results further suggest that a stoichiometric single-u.c. STO^5-SRO^1-STO^5 heterostructure would be FM and metallic. However, we observed that SRO in STO^5-SRO^1-STO^5 is nonstoichiometric, exhibiting a much greater amount of Ti in the SRO blocks due to Ti-Ru

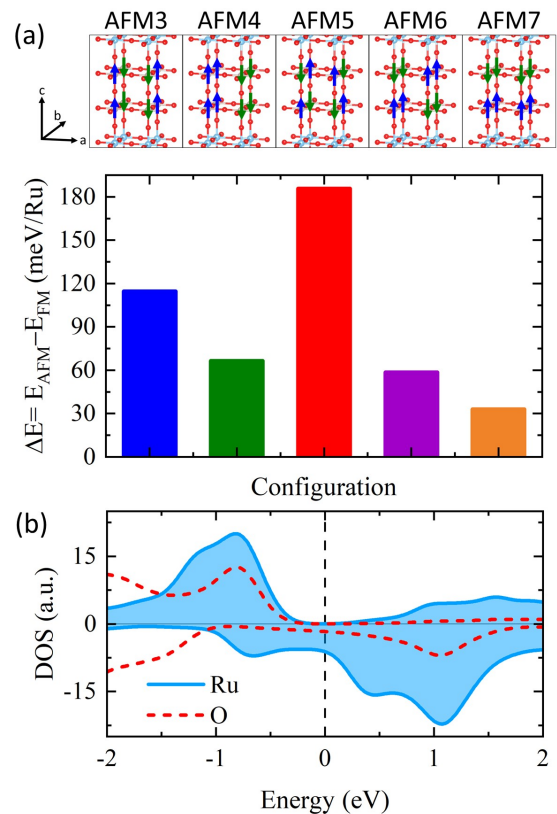FIG. 9. (a) Possible AFM arrangements for the Ru sublattice in the STO^5-SRO^2-STO^5 heterostructure and their relative energy per Ru atom compared to the FM ground state. (b) Density of states for the lower RuO_2 plane in the STO^5-SRO^2-STO^5 heterostructure.

intermixture than in the STO^5-SRO^2-STO^5 heterostructure. The existence of these nonmagnetic Ti impurities in single-u.c. SRO drastically affects the electronic structure as well as the coherence for FM ordering. Therefore, we conclude that it is the off-stoichiometry dictated by the Ti-Ru intermixture that leads to the insulating and non-FM behavior of SRO in the single-u.c. thickness limit. The experimental data of Refs. [32,33,36] that find the single-u.c. SRO film to be FM confirm our overall conclusions about both STO^5-SRO^1-STO^5 and STO^5-SRO^2-STO^5 heterostructures.

APPENDIX: COMPUTATIONAL DETAILS

The Vienna *Ab initio* Simulation Package (VASP) [58] was used to perform density-functional theory calculations utilizing the projector augmented-wave method to describe core-valence electron interactions [59,60]. The Perdew-Burke-Ernzerhof generalized gradient approximation [61] with a Hubbard U correction (discussed in detail below) [62] was employed for the exchange-correlation functional. For the heterostructure calculations, a plane-wave basis cutoff energy of 450 eV was used and the Brillouin zone was sampled using a $4 \times 4 \times 1$ Γ-centered k-point grid. The heterostructures considered were terminated with SrO on both sides and consisted of five layers of TiO_2 on each side of the inserted RuO_2 layers. Each layer consists of a 2×2 lateral supercell of the cubic cell (four Ru sites). For the consideration of 25% Ti substitution for Ru, a 2×2 lateral supercell of the previous structure was used (16 Ru sites before substitution). A vacuum spacing of 15 Å was used to prevent spurious interactions due to periodic boundary conditions along the z axis. All structures were relaxed until the atomic forces were converged to less than 0.02 eV/Å.

The electronic structure of bulk $SrRuO_3$ (SRO) according to Rondinelli *et al.* [28] is best described by including electron-electron correlations in the form of a Hubbard term with $U = 0.6$ eV. For Hubbard U values > 2 eV, in bulk, SRO becomes half metallic [28,63,64]. For SRO ultrathin films, theoretical calculations even with $U > 3$ eV are incapable to reproduce the observed insulating-nonmagnetic state [28]. Due to these observations, Rondinelli *et al.* [28] concluded that the insulating-nonmagnetic state is not caused by intrinsic changes such as enhanced electron interactions or structural changes, but rather triggered by surface roughness, defects, or disorder. However, according to Verissimo *et al.* [32], the single layer of Ru confined between STO lattice is a minority-spin half-metallic ferromagnet with $U = 4$ eV. Furthermore, recent calculations using a Hubbard U of 3.5 eV produced the most reasonable results for few-layer SRO films sandwiched between $BaTiO_3$ in thin-film heterostructures [18]. Therefore, we adopted Hubbard $U = 3.5$ eV in the present study of the STO^5-SRO^n-STO^5 heterostructures. Variation of the effective Hubbard U by ± 0.5 eV does not change the qualitative results when tested on the stoichiometric STO^5-SRO^1-STO^5 heterostructure (i.e., it remains a ferromagnetic metal).

[1] A. Brinkman, M. Huijben, M. Van Zalk, J. Huijben, U. Zeitler, J. C. Maan, W. G. Van Der Wiel, G. Rijnders, D. H. A. Blank, and H. Hilgenkamp, Magnetic effects at the interface between non-magnetic oxides, Nat. Mater. **6**, 493 (2007).

[2] P. Zubko, S. Gariglio, M. Gabay, P. Ghosez, and J.-M. Triscone, Interface physics in complex oxide heterostructures, Annu. Rev. Condens. Matter Phys. **2**, 141 (2011).

[3] A. Bhattacharya and S. J. May, Magnetic oxide heterostructures, Annu. Rev. Mater. Res. **44**, 65 (2014).

[4] R. Ramesh and D. G. Schlom, Creating emergent phenomena in oxide superlattices, Nat. Rev. Mater. **4**, 257 (2019).

[5] J. Wang, J. B. Neaton, H. Zheng, V. Nagarajan, S. B. Ogale, B. Liu, D. Viehland, V. Vaithyanathan, D. G. Schlom, U. V. Waghmare, N. A. Spaldin, K. M. Rabe, M. Wuttig, and R. Ramesh, Epitaxial BiFeO₃ multiferroic thin film heterostructures, Science **299**, 1719 (2003).

[6] A. Ohtomo and H. Y. Hwang, A high-mobility electron gas at the LaAlO₃/SrTiO₃ heterointerface, Nature (London) **427**, 423 (2004).

[7] W. Wang, M. W. Daniels, Z. Liao, Y. Zhao, J. Wang, G. Koster, G. Rijnders, C.-Z. Chang, D. Xiao, and W. Wu, Spin chirality fluctuation in two-dimensional ferromagnets with perpendicular magnetic anisotropy, Nat. Mater. **18**, 1054 (2019).

[8] J. P. Ruf, H. Paik, N. J. Schreiber, H. P. Nair, L. Miao, J. K. Kawasaki, J. N. Nelson, B. D. Faeth, Y. Lee, B. H. Goodge, B. Pamuk, C. J. Fennie, L. F. Kourkoutis, D. G. Schlom, and K. M. Shen, Strain-stabilized superconductivity, Nat. Commun. **12**, 59 (2021).

[9] R. Scherwitzl, S. Gariglio, M. Gabay, P. Zubko, M. Gibert, and J. M. Triscone, Metal-Insulator Transition in Ultrathin LaNiO₃ Films, Phys. Rev. Lett. **106**, 246403 (2011).

[10] Z. Liao, F. Li, P. Gao, L. Li, J. Guo, X. Pan, R. Jin, E. W. Plummer, and J. Zhang, Origin of the metal-insulator transition in ultrathin films of La₂/₃Sr₁/₃MnO₃, Phys. Rev. B: Condens. Matter Mater. Phys. **92**, 125123 (2015).

[11] Y. J. Chang, C. H. Kim, S. H. Phark, Y. S. Kim, J. Yu, and T. W. Noh, Fundamental Thickness Limit of Itinerant Ferromagnetic SrRuO₃ Thin Films, Phys. Rev. Lett. **103**, 057201 (2009).

[12] C. W. Jones, P. D. Battle, P. Lightfoot, and W. T. A. Harrison, The structure of SrRuO₃ by time-of-flight neutron powder diffraction, Acta Crystallogr., Sect. C: Cryst. Struct. Commun. **45**, 365 (1989).

[13] A. Callaghan, C. W. Moeller, and R. Ward, Magnetic interactions in ternary ruthenium oxides, Inorg. Chem. **5**, 1572 (1966).

[14] R. J. Bouchard and J. L. Gillson, Electrical properties of CaRuO3 and SrRuO₃ single crystals, Mater. Res. Bull. **7**, 873 (1972).

[15] D. Kan, R. Aso, R. Sato, M. Haruta, H. Kurata, and Y. Shimakawa, Tuning magnetic anisotropy by interfacially engineering the oxygen coordination environment in a transition metal oxide, Nat. Mater. **15**, 432 (2016).

[16] K. Takiguchi, Y. K. Wakabayashi, H. Irie, Y. Krockenberger, T. Otsuka, H. Sawada, S. A. Nikolaev, H. Das, M. Tanaka, Y. Taniyasu, and H. Yamamoto, Quantum transport evidence of Weyl fermions in an epitaxial ferromagnetic oxide, Nat. Commun. **11**, 4969 (2020).

[17] G. Koster, L. Klein, W. Siemons, G. Rijnders, J. S. Dodge, C. B. Eom, D. H. A. Blank, and M. R. Beasley, Structure, physical properties, and applications of SrRuO₃ thin films, Rev. Mod. Phys. **84**, 253 (2012).

[18] M. Meng, Z. Wang, A. Fathima, S. Ghosh, M. Saghayezhian, J. Taylor, R. Jin, Y. Zhu, S. T. Pantelides, J. Zhang, E. W.

Plummer, and H. Guo, Interface-induced magnetic polar metal phase in complex oxides, Nat. Commun. **10**, 5248 (2019).

[19] P. Siwakoti, Z. Wang, M. Saghayezhian, D. Howe, Z. Ali, Y. Zhu, and J. Zhang, Abrupt orthorhombic relaxation in compressively strained ultra-thin SrRuO₃ films, Phys. Rev. Mater. **5**, 114409 (2021).

[20] J. Xia, W. Siemons, G. Koster, M. R. Beasley, and A. Kapitulnik, Critical thickness for itinerant ferromagnetism in ultrathin films of SrRuO₃, Phys. Rev. B: Condens. Matter Mater. Phys. **79**, 2 (2009).

[21] K. Ishigami, K. Yoshimatsu, D. Toyota, M. Takizawa, T. Yoshida, G. Shibata, T. Harano, Y. Takahashi, T. Kadono, V. K. Verma, V. R. Singh, Y. Takeda, T. Okane, Y. Saitoh, H. Yamagami, T. Koide, M. Oshima, H. Kumigashira, and A. Fujimori, Thickness-dependent magnetic properties and strain-induced orbital magnetic moment in SrRuO₃ thin films, Phys. Rev. B: Condens. Matter Mater. Phys. **92**, 3 (2015).

[22] M. Izumi, K. Nakazawa, and Y. Bando, TC suppression of SrRuO₃/SrTiO₃ superlattices, J. Phys. Soc. Jpn. **67**, 651 (1998).

[23] M. Izumi, K. Nakazawa, Y. Bando, Y. Yoneda, and H. Terauchi, Magnetic properties of SrRuO₃/SrTiO₃ superlattices, Solid State Ionics **108**, 227 (1998).

[24] F. Bern, M. Ziese, A. Setzer, E. Pippel, D. Hesse, and I. Vrejoiu, Structural, magnetic and electrical properties of SrRuO₃ Films and SrRuO₃/SrTiO₃ superlattices, J. Phys.: Condens. Matter **25**, 496003 (2013).

[25] D. Toyota, I. Ohkubo, H. Kumigashira, M. Oshima, T. Ohnishi, M. Lippmaa, M. Takizawa, A. Fujimori, K. Ono, M. Kawasaki, and H. Koinuma, Thickness-dependent electronic structure of ultrathin SrRuO₃ films studied by in situ photoemission spectroscopy, Appl. Phys. Lett. **87**, 162508 (2005).

[26] D. Toyota, I. Ohkubo, H. Kumigashira, M. Oshima, T. Ohnishi, M. Lippmaa, M. Kawasaki, and H. Koinuma, Ferromagnetism stabilization of ultrathin SrRuO₃ Films: Thickness-dependent physical properties, J. Appl. Phys. **99**, 08N505 (2006).

[27] X. Shen, X. Qiu, D. Su, S. Zhou, A. Li, and D. Wu, Thickness-dependent metal-insulator transition in epitaxial SrRuO₃ ultrathin films, J. Appl. Phys. **117**, 015307 (2015).

[28] J. M. Rondinelli, N. M. Caffrey, S. Sanvito, and N. A. Spaldin, Electronic properties of bulk and thin film SrRuO₃: Search for the metal-insulator transition, Phys. Rev. B: Condens. Matter Mater. Phys. **78**, 1 (2008).

[29] C. Autieri, Antiferromagnetic and *xy* ferro-orbital order in insulating SrRuO₃ thin films with SrO termination, J. Phys.: Condens. Matter **28**, 426004 (2016).

[30] L. Si, Z. Zhong, J. M. Tomczak, and K. Held, Route to room-temperature ferromagnetic ultrathin SrRuO₃ films, Phys. Rev. B: Condens. Matter Mater. Phys. **92**, 1 (2015).

[31] K. Gupta, B. Mandal, and P. Mahadevan, Strain-induced metal-insulator transition in ultrathin films of SrRuO₃, Phys. Rev. B: Condens. Matter Mater. Phys. **90**, 1 (2014).

[32] M. Verissimo-Alves, P. García-Fernández, D. I. Bilc, P. Ghosez, and J. Junquera, Highly Confined Spin-Polarized Two-Dimensional Electron Gas in SrTiO₃/SrRuO₃ Superlattices, Phys. Rev. Lett. **108**, 107003 (2012).

[33] B. Sohn, J. R. Kim, C. H. Kim, S. Lee, S. Hahn, Y. Kim, S. Huh, D. Kim, Y. Kim, W. Kyung, M. Kim, M. Kim, T. W.

Noh, and C. Kim, Observation of metallic electronic structure in a single-atomic-layer oxide, Nat. Commun. **12**, 6171 (2021).

[34] S. H. Chang, Y. J. Chang, S. Y. Jang, D. W. Jeong, C. U. Jung, Y. J. Kim, J. S. Chung, and T. W. Noh, Thickness-dependent structural phase transition of strained SrRuO₃ ultrathin films: The role of octahedral tilt, Phys. Rev. B: Condens. Matter Mater. Phys. **84**, 1 (2011).

[35] Z. Cui, A. J. Grutter, H. Zhou, H. Cao, Y. Dong, D. A. Gilbert, J. Wang, Y.-S. Liu, J. Ma, Z. Hu, J. Guo, J. Xia, B. J. Kirby, P. Shafer, E. Arenholz, H. Chen, X. Zhai, and Y. Lu, Correlation-driven eightfold magnetic anisotropy in a two-dimensional oxide monolayer, Sci. Adv. **6**, eaay0114 (2020).

[36] H. Boschker, T. Harada, T. Asaba, R. Ashoori, A. V. Boris, H. Hilgenkamp, C. R. Hughes, M. E. Holtz, L. Li, D. A. Muller, H. Nair, P. Reith, X. Renshaw Wang, D. G. Schlom, A. Soukiassian, and J. Mannhart, Ferromagnetism and Conductivity in Atomically Thin SrRuO₃, Phys. Rev. X **9**, 011027 (2019).

[37] J. M. Rondinelli, S. J. May, and J. W. Freeland, Control of octahedral connectivity in perovskite oxide heterostructures: An emerging route to multifunctional materials discovery, MRS Bull. **37**, 261 (2012).

[38] E. J. Moon, Q. He, S. Ghosh, B. J. Kirby, S. T. Pantelides, A. Y. Borisevich, and S. J. May, Structural "δ Doping" to Control Local Magnetization in Isovalent Oxide Heterostructures, Phys. Rev. Lett. **119**, 197204 (2017).

[39] S. J. May, C. R. Smith, J. W. Kim, E. Karapetrova, A. Bhattacharya, and P. J. Ryan, Control of octahedral rotations in (LaNiO₃)ⁿ/(SrMnO₃)ᵐ superlattices, Phys. Rev. B: Condens. Matter Mater. Phys. **83**, 2 (2011).

[40] N. Nakagawa, H. Y. Hwang, and D. A. Muller, Why some interfaces cannot be Sharp, Nat. Mater. **5**, 204 (2006).

[41] L. Capogna, A. P. Mackenzie, A. P. Mackenzie, R. S. Perry, S. A. Grigera, L. M. Galvin, P. Raychaudhuri, A. J. Schofield, C. S. Alexander, G. Cao, S. R. Julian, and Y. Maeno, Sensitivity to Disorder of the Metallic State in the Ruthenates, Phys. Rev. Lett. **88**, 076602 (2002).

[42] H. P. Nair, Y. Liu, J. P. Ruf, N. J. Schreiber, S. L. Shang, D. J. Baek, B. H. Goodge, L. F. Kourkoutis, Z. K. Liu, K. M. Shen, and D. G. Schlom, Synthesis science of SrRuO₃ and CaRuO₃ epitaxial films with high residual resistivity ratios, APL Mater. **6**, 046101 (2018).

[43] W. Siemons, G. Koster, A. Vailionis, H. Yamamoto, D. H. A. Blank, and M. R. Beasley, Dependence of the electronic structure of SrRuO₃ and its degree of correlation on cation off-stoichiometry, Phys. Rev. B: Condens. Matter Mater. Phys. **76**, 075126 (2007).

[44] B. I. Shklovskii and A. L. Efros, *Electronic Properties of Doped Semiconductors* (Springer, Berlin, 1984), Vol. 45.

[45] V. F. Gantmakher and L. I. Man, *Electrons and Disorder in Solids* (Oxford University Press, Oxford, 2005).

[46] D. C. Licciardello and D. J. Thouless, Constancy of Minimum Metallic Conductivity in Two Dimensions, Phys. Rev. Lett. **35**, 1475 (1975).

[47] N. E. Hussey, K. Takenaka, and H. Takagi, Universality of the Mott–Ioffe–Regel limit in metals, Philos. Mag. **84**, 2847 (2007).

[48] P. A. Lee and T. V. Ramakrishnan, Disordered electronic systems, Rev. Mod. Phys. **57**, 287 (1985).

[49] N. Furukawa, Transport properties of the Kondo lattice model in the limit $S = \infty$ and $D = \infty$, J. Phys. Soc. Jpn. **63**, 3214 (1994).

[50] Y. Tokura, A. Urushibara, T. Arima, Y. Moritomo, A. Asamitsu, G. Kido, and N. Furukawa, Giant magnetotransport phenomena in filling-controlled Kondo lattice system: $La_{1-x}Sr_xMnO_3$, J. Phys. Soc. Jpn. **63**, 3931 (1994).

[51] J. Fontcuberta, B. Martínez, A. Seffar, S. Piñol, J. L. García-Muñoz, and X. Obradors, Colossal Magnetoresistance of Ferromagnetic Manganites: Structural Tuning and Mechanisms, Phys. Rev. Lett. **76**, 1122 (1996).

[52] Y. Tomioka, A. Asamitsu, and Y. Tokura, Magnetotransport properties and magnetostructural phenomenon in single crystals of $La_{0.7}(Ca_{1-y}Sr_y)MnO_3$, Phys. Rev. B: Condens. Matter Mater. Phys. **63**, 024421 (2001).

[53] J. Wu, J. W. Lynn, C. J. Glinka, J. Burley, H. Zheng, J. F. Mitchell, and C. Leighton, Intergranular Giant Magnetoresistance in a Spontaneously Phase Separated Perovskite Oxide, Phys. Rev. Lett. **94**, 037201 (2005).

[54] J. Q. Xiao, J. S. Jiang, and C. L. Chien, Giant Magnetoresistance in Nonmultilayer Magnetic Systems, Phys. Rev. Lett. **68**, 3749 (1992).

[55] L. M. Wang, H. E. Horng, and H. C. Yang, Anomalous magnetotransport in $SrRuO_3$ Films: A crossover from Fermi-liquid to non-Fermi-liquid behavior, Phys. Rev. B: Condens. Matter Mater. Phys. **70**, 014433 (2004).

[56] D. B. Kacedon, R. A. Rao, and C. B. Eom, Magnetoresistance of epitaxial thin films of ferromagnetic metallic oxide $SrRuO_3$ with different domain structures, Appl. Phys. Lett. **71**, 1724 (1997).

[57] L. F. Kourkoutis, J. H. Song, H. Y. Hwang, and D. A. Muller, Microscopic origins for stabilizing room-temperature ferromagnetism in ultrathin manganite layers, Proc. Natl. Acad. Sci. USA **107**, 11682 (2010).

[58] G. Kresse and J. Furthmüller, Efficient iterative schemes for ab initio total-energy calculations using a plane-wave basis set, Phys. Rev. B: Condens. Matter Mater. Phys. **54**, 11169 (1996).

[59] P. E. Blöchl, Projector augmented-wave method, Phys. Rev. B **50**, 17953 (1994).

[60] G. Kresse and D. Joubert, From ultrasoft pseudopotentials to the projector augmented-wave method, Phys. Rev. B **59**, 1758 (1999).

[61] J. P. Perdew, K. Burke, and M. Ernzerhof, Generalized Gradient Approximation Made Simple, Phys. Rev. Lett. **77**, 3865 (1996).

[62] S. Dudarev and G. Botton, Electron-energy-loss spectra and the structural stability of nickel oxide: An LSDA+U study, Phys. Rev. B: Condens. Matter Mater. Phys. **57**, 1505 (1998).

[63] D. J. Singh, Electronic and magnetic properties of the 4d itinerant ferromagnet $SrRuO_3$, J. Appl. Phys. **79**, 4818 (1996).

[64] I. Mazin and D. Singh, Electronic structure and magnetism in Ru-based perovskites, Phys. Rev. B: Condens. Matter Mater. Phys. **56**, 2556 (1997).